Thermal debonding of inclusions in compacted graphite iron: Effect of matrix phases

Thermal debonding of inclusions in compacted graphite iron: Effect of matrix phases

Evangelia Nektaria Palkanoglou, Konstantinos P. Baxevanakis [*], Vadim V. Silberschmidt

Wolfson School of Mechanical, Electrical and Manufacturing Engineering, Loughborough University, LE11 3TU, UK

A B S T R A C T

This paper investigates graphite decohesion as the primary fracture mechanism of compacted graphite iron (CGI) subjected to thermal load. Despite CGI's extensive industrial use and considerable research on its mechanical behaviour, thermal debonding is not yet fully understood, nor is the influence of matrix phases on it. After thermal cycling to confirm the occurrence of the phenomenon, a numerical approach is developed: a 2D unit cell is constructed, with a single graphite particle, represented as an ellipse embedded in a metallic matrix. The inclusion is surrounded by an extra layer that accounts for either pearlite or ferrite, in order to study their effect on thermal debonding. An elastoplastic behaviour is assumed for all constituents, described with a classical J2 flow theory of plasticity, and the models are analysed employing a finite-element approach. The proposed numerical strategy focuses on the influence of matrix phases on thermal debonding, identifying numerical schemes to assess it. The obtained results can provide significant knowledge on the response of CGI to thermal load at the microscale, contributing to the understanding of its macroscopic thermomechanical behaviour.

1. Introduction

Since its discovery in 1948 [1], compacted graphite iron (CGI) became a substitution for grey iron in various industrial applications, such as pipes and machinery, as well as in automotive industry, either in brakes or parts of car engines. CGI seems to be a better option than grey iron thanks to its improved thermal and mechanical properties, its superior casting qualities, as well as its competitive price. CGI is a ferrous alloy, which major alloying elements are iron, carbon (in the form of graphite or carbide), and silicon. CGI's microstructure is characterised by the presence of graphite particles of different shapes and sizes embedded in a metallic matrix. The matrix can be either fully pearlitic/ferritic or a combination of the two phases; each of these three cases alters the macroscopic thermal and mechanical properties of the material.

Despite its extensive industrial use, the fracture of CGI at the microscale is not yet fully understood. Graphite inclusions seem to play a significant part in the fracture of CGI. Being very soft and brittle, with a low coefficient of thermal expansion (CTE), graphite inclusions cannot expand to the same extent and at the same rate as their surrounding matrix. The mismatch in the deformation ability of the two constituents can cause the decohesion of inclusions from the surrounding matrix [2,3]. Such debonding not only significantly decreases the loading capacity of the microstructure, since the debonded inclusions cannot bear any additional load, but can

---

* Corresponding author.
  E-mail address: K.Baxevanakis@lboro.ac.uk (K.P. Baxevanakis).

also trigger the initiation of microcracks. Such microcracks can then coalesce creating larger cracks propagating along the interface and in the matrix, eventually causing a network of cracks leading to total failure [2–5].

Debonding was experimentally confirmed as the main fracture mechanism in cast irons at the microscale, mainly under tensile or cyclic loading conditions [6–8]. Under uniaxial tensile load, debonding was observed in ductile cast irons at a stress level of around 320 MPa for a ferritic matrix and above 770 MPa for a pearlitic one [4,9,10]. Graphite decohesion was also identified for CGI in experiments where the exposure to high temperature was followed by a tensile load. In such cases, the thermal loading softened the microstructure and, as a result, decohesion appeared before the stress level in the matrix reached 50 MPa [5]. In the case of cyclic loading, graphite nodules in ductile cast iron may also lose their contact with the surrounding matrix either partially or completely [8,9,11–13].

Although graphite decohesion was verified experimentally for mechanical loads, its identification under purely thermal load and the investigation of the parameters that affect it are still not complete. Thermal debonding may be triggered by the mismatch in deformation capacity between graphite and surrounding matrix due to their different responses to thermal loading. Various parameters can influence this phenomenon, such as the morphology of inclusions, the phases of the surrounding matrix, etc.; however, very few of them were studied thoroughly and mostly for ductile iron under mechanical load. The effect of matrix phases on particle decohesion was investigated for tensile loading [6] but there is no study for a purely thermal load. Having different mechanical properties and deformational capacity, pearlite and ferrite may either decelerate or accelerate the onset of decohesion, thus improving or deteriorating the performance of microstructure in such conditions.

Generally, matrix phases are rarely considered as *pearlite* or *ferrite* in phenomenological or micromechanical modelling schemes. When employing the former approach, no distinction of the constituents is required since this method focuses on the description of the macroscopic behaviour of the material by modifying the yield surface and the hardening parameter to account for microstructural features and fracture mechanisms [14–19]. On the other hand, most micromechanical models focus primarily on either direct incorporation of CGI's microstructure [20–22] or modelling the graphite inclusions by assuming either elastoplastic [23] or anisotropic [24] behaviour. To identify the influence of different assumptions for the inclusions on microstructural response, no different phases were considered for the surrounding matrix for simplicity; as a result, the matrix was assumed to be ferritic, exhibiting an elastoplastic behaviour.

As already discussed, CGI is vulnerable at high temperatures due to the mismatch in the CTE of its constituents. Despite the large number of CGI applications at high temperatures, thermal debonding was not thoroughly studied experimentally or numerically, mainly due to the complexity of its microstructure, which is difficult to characterise and model. Therefore, this paper focuses on graphite decohesion under purely thermal load, assessing the influence of matrix phases on its initiation and further propagation. This is accomplished through experiments to confirm thermal debonding and the effect of matrix phases on its development as well as with a numerical methodology to model the phenomenon. The necessary inputs for the models are obtained from statistical analysis of SEM micrographs, mechanical testing at various temperatures, and nano-indentation testing.

2. Methodology

2.1. Experimental procedures and findings

To confirm experimentally the effect of different matrix phases on thermal debonding of graphitic inclusions, a specimen made of EN-GJV-450 was used. Its chemical composition and macroscopic properties are listed in Tables 1 and 2, respectively. A typical short cylindrical sample with diameter 20 mm and length 10 mm was machined with a wet abrasive cutting machine. After machining, it was subjected to grinding with two different grit sizes, P500 (30.2 μm grit size) and P1200 (15.3 μm). Finally, the sample was polished using polishing cloths with different abrasive sizes starting from 9 μm to less than 1 μm.

The specimen was subjected to four thermal cycles from room temperature up to 500 °C and back to room temperature with heating and cooling rates equivalent to 240 °C/hr and 120 °C/hr. The specimen was examined after each cycle using optical microscopy. Chemical etching was essential after each cycle to remove oxidation produced during the thermal cycle and allow for better observation of decohesions.

Before loading the specimens with thermal cycles, their surface was characterised using optical microscopy, in order to identify the interfacial areas where graphite, pearlite, and ferrite coexist (Fig. 1) and monitor them during the cycles. Three different morphologies of inclusions can be identified in the microstructure: *nodular*, *vermicular*, and *flake* graphite. Nodular particles tend to have a spherical shape, flakes are very long and thin, and vermiculars correspond to an intermediate shape between flake and nodular.

Nodular inclusions allow a better investigation of the effect of the ferritic layer on their debonding thanks to their morphology that enables the ferritic growth to form a thick ring around them [26]. Such graphite particles tended to debond earlier compared to those surrounded by a pearlitic layer. Although both pearlite and ferrite have the CTE of the same magnitude (an order of magnitude larger

Table 1
Chemical composition (%) of EN-GJV-450.

Fe	C	Si	Cu	Mn	Sn	Cr	Ni	S
92	3.8	2.42	0.917	0.297	0.083	0.025	0.023	0.013
P	Ce	Mg	Al	Ti	V	Mo	Nb	
0.01	0.01	0.009	0.008	0.009	0.008	0.001	0.002	

Table 2
Macroscopic properties of EN-GJV-450 [25].

Property	23 °C	100 °C	400 °C
Ultimate tensile strength (MPa)	450–525	425–500	350–425
0.2% proof stress (MPa)	315–365	290–340	265–315
Elongation (%)	1–2.5	1–2	0.5–1.5
Elastic modulus (GPa)	144–155	140–150	135–145
Thermal conductivity (W/mK)	38	37	36
CTE (10^{-6} per °C)	11	11	12.5
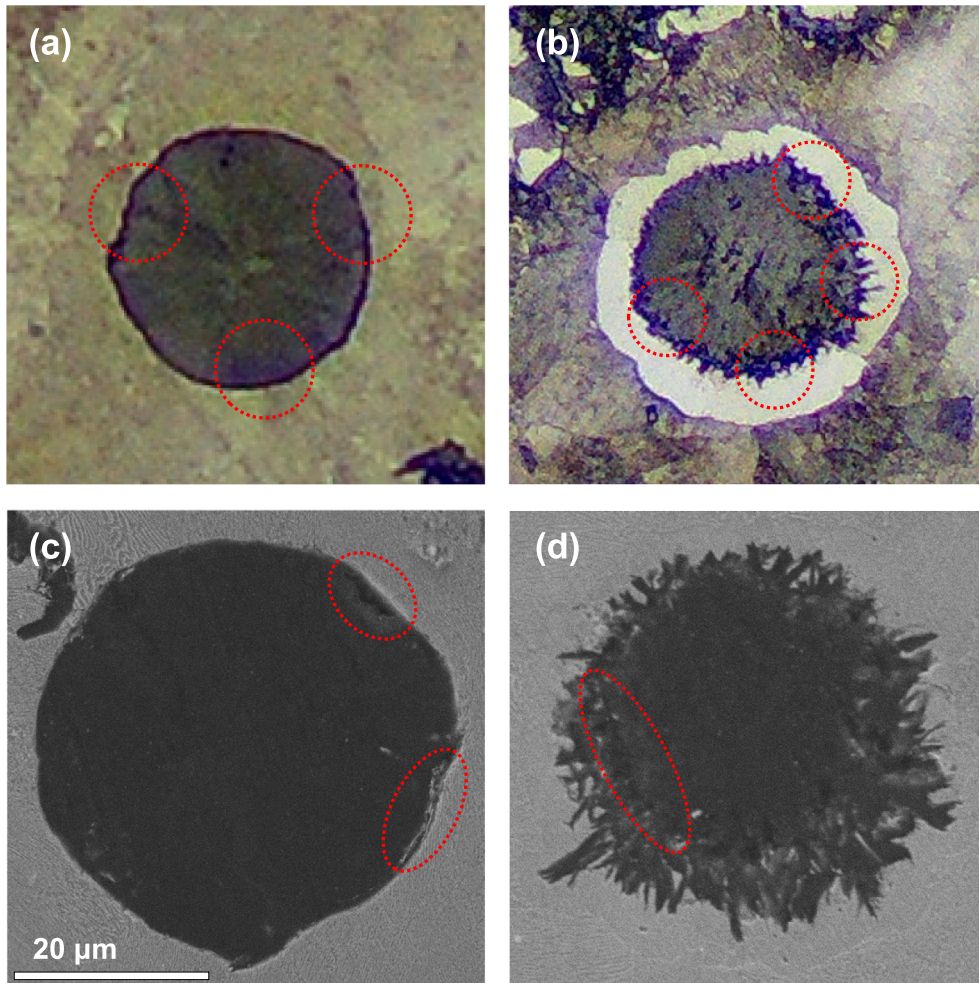
Fig. 1. Debonded graphite nodules obtained with optical microscopy (upper row) and SEM (lower row) surrounded by pearlite (a)-(c) and ferrite (b)-(d) after four thermal cycles (red dotted lines show areas of interfacial debonding).

than that of graphite), the latter phase is much softer and deformable compared to the former. Therefore, higher strains were observed in expansions due to the applied thermal load, causing the initiation of debonding mechanism in the first thermal cycle (Fig. 1 (b) and (d)). On the other hand, pearlite is much stiffer, so its deformations were limited during expansion, and debonding was observed after four thermal cycles (Fig. 1 (a) and (c)).

2.2. Microstructure-based modelling

2.2.1. Geometry

Based on the micrographs obtained in the thermal experiment, a two-dimensional model was developed with four different domains: *graphite*, *interface*, *ferrite/pearlite*, and *remaining matrix area* (Fig. 2). Although only ferrite forms thick layers around nodular and vermicular inclusions, this configuration was also used for pearlite in this model for comparison purposes, in order to study the effect of

both phases on graphite debonding. While, in general, a unit cell encloses many inclusions [27], a single-inclusion representative volume element (RVE) was selected here. Due to CGI's complex microstructure, the effect of different matrix phases on graphite debonding could not be decoupled from the interaction between the particles. However, effective properties were assumed for the rest of the metallic matrix to account for the existence of particles. Finally, an interface was incorporated between the inclusion and the ferritic/pearlitic domain in order to investigate decohesion thoroughly.

Following these assumptions, the model was generated comprising either a nodular or an elliptical inclusion corresponding to graphite embedded in a square RVE. Vermicular particles have a complex morphology in three dimensions. Their shape resembles more an oblate spheroid rather than an ellipsoid [28,29]. However, their cross-section in two dimensions can be effectively assumed to be an ellipse.

Additionally, a very thin layer around the inclusion was also established, representing the interface. After performing a parametric analysis for the interfacial thickness, the value of this parameter was selected to be 1 μm, in order not to affect the quality of numerical results [30]. Matrix phases were considered as another, thicker layer around the interfacial one. The thickness of the ferritic layer was obtained after performing statistical analysis on selected micrographs and calculating the mean value of the measured layer thicknesses.

Finally, the remaining microstructure was taken into consideration by applying the effective properties of CGI to the remaining area of the RVE. Flake particles were not studied here because ferrite tends to concentrate on their sharp edges creating ferritic neighbourhoods instead of ferrite layers fully surrounding them. Hence, no direct comparison with nodular and vermicular inclusions could be performed. All the dimensions of the constituents were selected to be in full accordance with microstructural characterisation performed for this material [30]. The volume fraction of graphite was assumed to be 8.2% based on the results of this characterisation [30].

2.2.2. Constitutive relations

Being a soft metal, ferrite can be described as an isotropic ductile material; hence, assuming an elastoplastic behaviour, a classical J_2 flow theory of plasticity was used herein for its constitutive description. On the other hand, pearlite is a heterogeneous material made as a lamellar structure comprising consecutive layers of ferrite and cementite. However, it is a common practice when dealing with composites to substitute an inhomogeneous phase such as pearlite with a 'homogenised' medium, with properties derived directly from the properties of the individual constituents and microstructure. Therefore, the J_2 flow theory of plasticity was also used to describe pearlite. Since thermal debonding was investigated, the Young's modulus, the CTE, and the plastic curve for both ferrite and pearlite were selected to be temperature-dependent.

Although the constitutive behaviour of both materials at room temperature is available in the literature, plastic stress-strain curves at high temperatures were found only for ferrite [31–32]. Hence, assumptions were made to introduce the temperature-dependent plastic stress-strain curves for pearlite. First, the renormalisation factor of the stress-strain curves of ferrite and pearlite at room temperature was calculated. Then, the stress-strain curves of pearlite at high temperatures were developed using this factor. Apart from the metallic phases of ferrite and pearlite in the model, graphite can be also described constitutively with the J_2 flow theory of plasticity. Despite its soft brittle nature, the literature has significant evidence that graphite exhibits a limited plastic behaviour [23,33,34]. The remaining area of the RVE was assigned with the macroscopic properties of CGI, derived from the mechanical testing of macroscopic specimens [30]. This assumption allowed the consideration of the contribution of other graphite particles in the microstructure. The selected values for all constitutive parameters for ferrite and pearlite are listed in Table 3, while the stress-strain
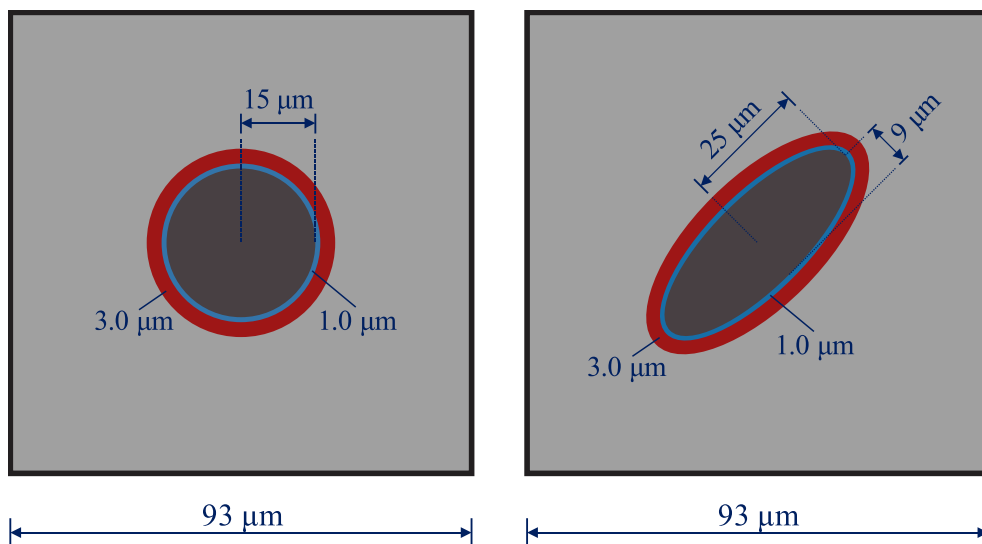

Fig. 2. Geometrical depiction of developed RVEs.

curves for all three constituents used in the model are depicted in Fig. 3. All the stress-strain curves used were obtained from mechanical testing performed on each constituent. The data for graphite were given in [33] and [34], whereas the mechanical properties for ferrite and pearlite were derived from [32]. Finally, the homogenised matrix properties were obtained with in-house mechanical testing.

Elastic constitutive law is described using tensorial notation as follows

$$\sigma_{ij} = C_{ijkl}\varepsilon_{kl} + \beta_{ij}(\theta - \theta_0),$$
(1)

where σ_{ij} and ε_{kl} are the stress and strain tensors, respectively, and C_{ijkl} is the stiffness tensor.

The decomposition of total strain into an elastic ε_{ij}^e and plastic ε_{ij}^p parts is given as

$$\varepsilon_{ij}^{tot} = \varepsilon_{ij}^e + \varepsilon_{ij}^p.$$
(2)

Assuming an isotropic hardening response, the yield function is given by

$$f(\sigma) = \sqrt{\frac{3}{2}\sigma_{ij}'\sigma_{ij}'} - (\sigma_Y - \mathrm{K}\,\sigma),$$
(3)

where σ_Y is the yield stress, K is the tangent modulus, and σ_{ij}' are the components of the deviatoric stress tensor.

Especially for the matrix phases and the homogenised matrix material, Eq. (3) was modified to the following form since the yield function was assumed to be temperature-dependent

$$f(\sigma) = \sqrt{\frac{3}{2}\sigma_{ij}'\sigma_{ij}'} - (\sigma_y(\theta) - K\sigma),$$
(4)

where θ denotes the temperature. A flow rule was also adjusted, given by

$$d\varepsilon^{pl} = d\dot{\bar{\varepsilon}}^{pl}\frac{3}{2}\frac{\sigma'}{\sqrt{\frac{3}{2}\sigma':\sigma'}},$$
(5)

where ε^{pl} and $\dot{\bar{\varepsilon}}^{pl}$ are the equivalent plastic strain and its rate, respectively.

To consider the debonding adequately, a traction-type elastic behaviour was applied to the interfacial layer surrounding graphite [30]. This was associated with a stress-based damage criterion leading to element deletion when its critical value was met. The values of the parameters of the criterion were selected in order for graphite to remain elastic during each thermal cycle [33] and are provided in Table 4. Damage estimation in a finite-element code was accomplished by calculating at each increment the magnitude of a damage variable (*D*) at all Gauss points of a finite element. This variable represents the fraction of stiffness reduction after initiation of material degradation. Hence, an element was characterised as damaged after *D* became nonzero in one of the four Gauss points, and element deletion took place when the critical value was exceeded at all integration points. The element deletion corresponded to the loss of contact between the matrix and the inclusion, after decohesion. The plastic behaviour of constituents was introduced into finite-element simulations using the stress-strain data presented in Fig. 3.

2.2.3. Boundary and loading conditions

Four-node plane stress elements (CPS4) were used to mesh the model. After conducting a mesh convergence study, 12,317 elements were used, leading to a total of 25,030 degrees of freedom. An RVE was considered as the smallest part of the microstructure that can be used to represent it in terms of its characteristics, assuming it has a regular pattern. To model the RVE adequately, continuity of both displacements and tractions across adjacent unit cells is required. This can only be ensured by the application of periodic boundary conditions (PBCs) at the RVE's edges, allowing accurate simulations of the deformation field [35]. Considering two points at opposing edges of a unit cell of length *d*, the periodic boundary conditions on them were stated as [35]

Table 3
Thermoelastic parameters of constituents used in simulations.

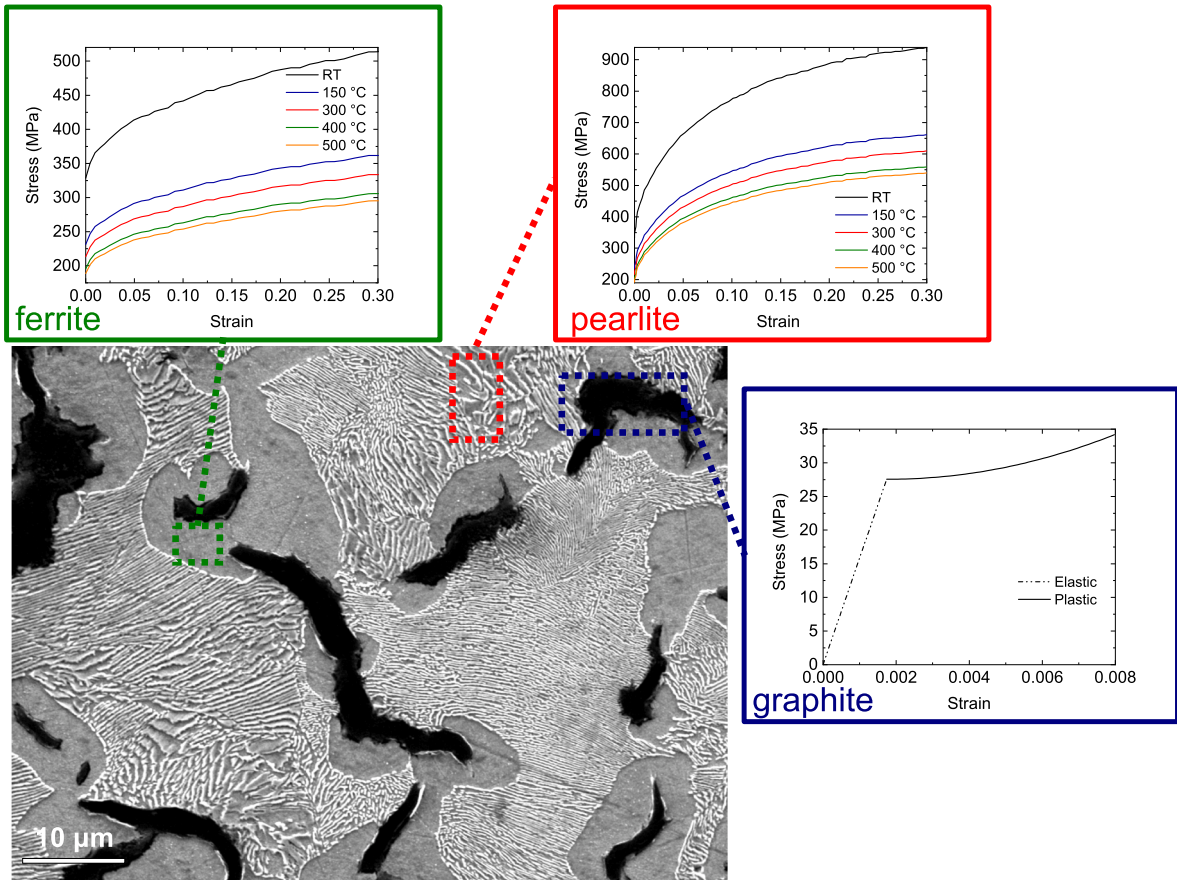| Graphite		Ferrite		Pearlite		Temperature (°C)
Young's modulus (GPa)	CTE (1/K)	Young's modulus (GPa)	CTE (1/K)	Young's modulus (GPa)	CTE (1/K)	
15.8	2.9E-06	211	1.12E-05	220.3	1.01E-05	25
		179.8	1.14E-05	195.8	1.03E-05	50
		169.0	1.20E-05	184.2	1.14E-05	100
		135.0	1.24E-05	150.1	1.20E-05	200
		150.0	1.33E-05	159.0	1.36E-05	300
		135.8	1.39E-05	142.2	1.43E-05	400
		108.0	1.42E-05	113.6	1.50E-05	500

Fig. 3. Stress-strain curves of constituents used in the model.

Table 4
Values of the parameters for damage criterion at the interfacial layer.

Normal nominal stress (GPa)	Displacement at failure (mm)	Softening type
2.5	0.009	Linear

$$\mathbf{u}(x, d) = \mathbf{u}(x) + \overline{\varepsilon}d, \tag{6}$$

$$\mathbf{t}(x, d) = -\mathbf{t}(x), \tag{7}$$

where $\mathbf{u}$ and $\mathbf{t}$ are the displacement and traction, respectively, and $\overline{\varepsilon}$ is the average infinitesimal strain over the volume.

To investigate thermal debonding, application of pure thermal loading was required to trigger this phenomenon. In this study, the unit cell was subjected to four thermal cycles. The temperature of the entire volume increased linearly from 25 °C to 500 °C and then decreased linearly back to 25 °C. Thermal cycles can be disastrous for CGI, due to its heterogeneous microstructure. There was no healing. Also, the residual stresses developed due to the mismatch of the CTEs of the two constituents can be added up after each cycle, causing an amplification of damage in the microstructure.

2.3. Model validation

The validation of the proposed modelling scheme was not a straightforward task, since the influence of matrix phases on thermal debonding was not investigated much before and no experimental data were found in the literature. Hence, validation was performed using the mechanical load. To this aim, experimental results from the literature [36], for a tensile load applied to spherical graphite particles, surrounded by either pearlitic or ferritic matrix material, were used for comparison with the numerical results obtained with the developed model.

According to the experimental data, decohesion from a pearlitic matrix initiated at 520 MPa, and a 60° angle arc at one side of the inclusion along the loading direction was the first debonded area. On the other hand, the onset of debonding for a nodular particle

surrounded by a ferritic matrix was first reported at 430 MPa. The debonded area formed a 25° angle arc somewhat away from the loading direction. The numerical results produced with the developed modelling scheme are depicted in Fig. 4. In both cases, the stress levels, as well as the sizes and positions of debonded areas, are in good agreement with the ones observed in the experiments.

3. Results

3.1. Evolution of plastic zone in RVE

The finite-element simulations demonstrated that the presence of ferrite or pearlite as a surrounding layer around graphite affected the initiation and further evolution of plastic strains in the RVE, as depicted in Fig. 5 and Fig. 6 (all graphs are plotted in the unde-formed configuration with the graphite domain removed). The equivalent plastic strain at each temperature level was normalised with the plastic strain at failure for the case of the layer around the nodular inclusion. A full model for the spherical inclusion was analysed instead of a quadrant for comparison purposes.

The layer surrounding the nodular graphite – ferritic or pearlitic – seems to have a protective effect on the remaining unit cell, as no plastic strains developed outside this layer. More specifically, no plasticisation was observed during the first thermal cycle for the pearlitic layer. Since the CTE for pearlite is slightly lower (compared to that of ferrite), the stresses induced due to the mismatch with graphite were lower and its yield point was higher compared to the homogenised material of the CGI matrix. Therefore, the stresses developed due to the thermomechanical mismatch were below the yield point and caused no plasticisation in the pearlitic domain (Fig. 5a). Although no plastic strains were observed during the second and third thermal cycles (Fig. 5b and c), they occurred during the fourth one, covering a very thin circular area at the inner circumference of the pearlitic layer (Fig. 5d). Taking into consideration the mechanical behaviour of pearlite, only residual stresses at the end of each cycle could trigger the appearance of plastic strains during the next thermal cycle. The residual stresses were far beyond the yield point; however, their magnitude seems to be amplified after each cycle, causing plastic strains to appear in the pearlitic layer during the fourth cycle (Fig. 7a). The magnitude of plastic strain was around 25% of the maximum plastic strain reported in the ferritic layer at 500 °C.

When a ferritic layer was around a nodular graphite, plasticisation did not initiate in the first cycle (Fig. 5e). Ferrite has a slightly higher yield point compared to that of the surrounding matrix so the stresses induced due to the mismatch of the CTEs between graphite and ferrite were below this point and could not cause plasticisation. However, the onset of plastic deformations was observed in the ferritic layer during the second cycle (Fig. 5f). As already discussed, only the residual stresses can cause the onset of plasticisation
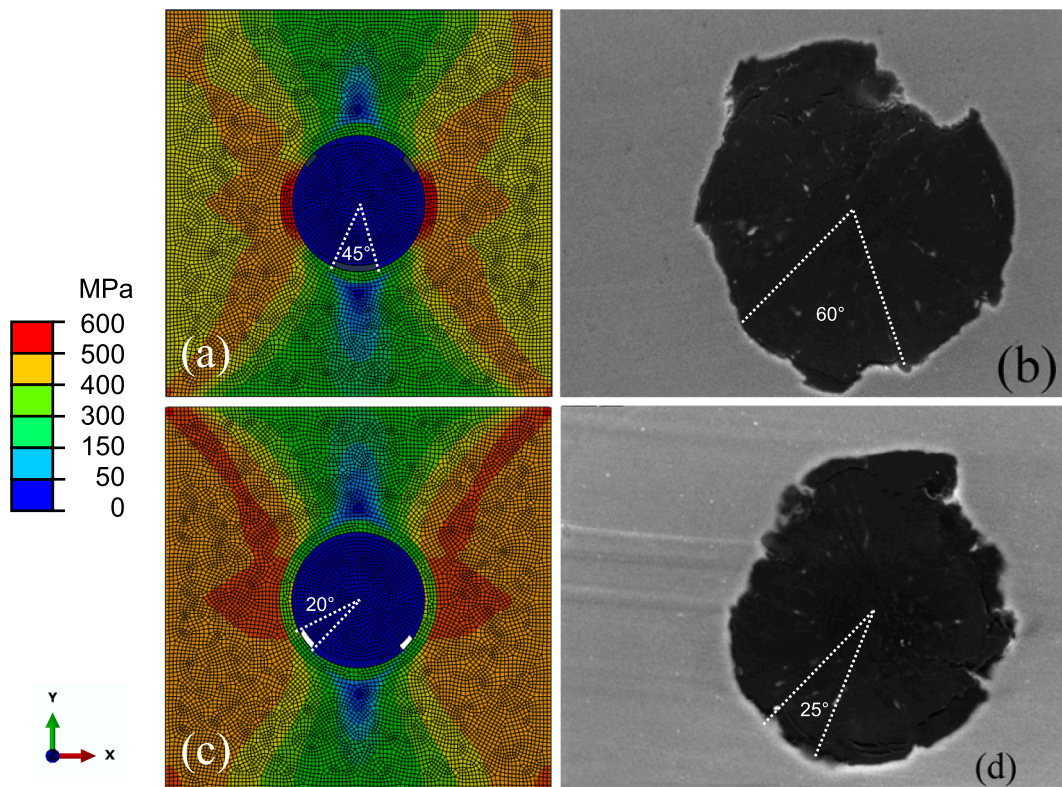

Fig. 4. Numerical data for the onset of decohesion for spherical graphite inclusion surrounded by pearlitic (a), (b) and ferritic (c), (d) matrix under tensile load (figures (b) and (d) from [36]).
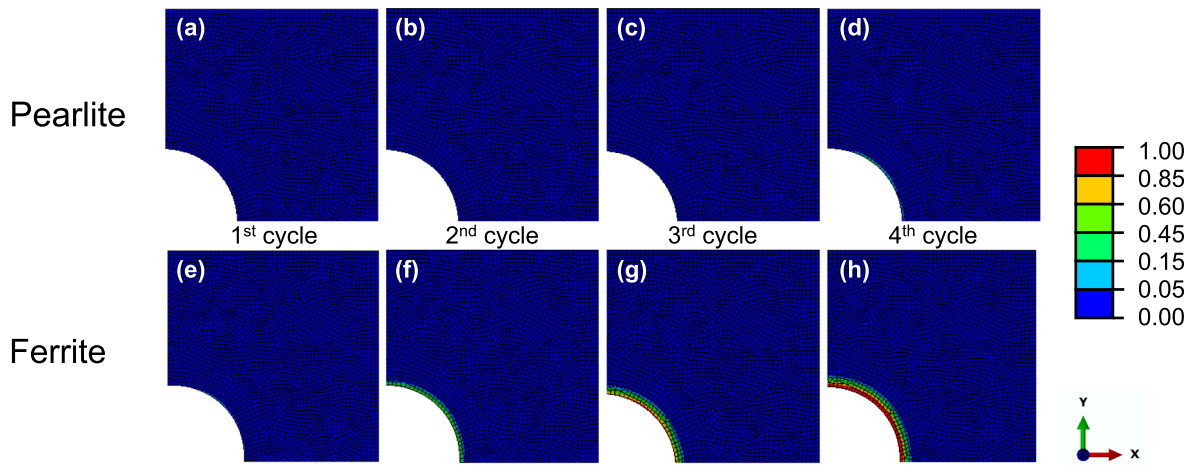
Fig. 5. Evolution of plastic zone in RVE with thermal cycles for nodular inclusion: (a)-(d) pearlitic layer; (e)-(h) ferritic layer.
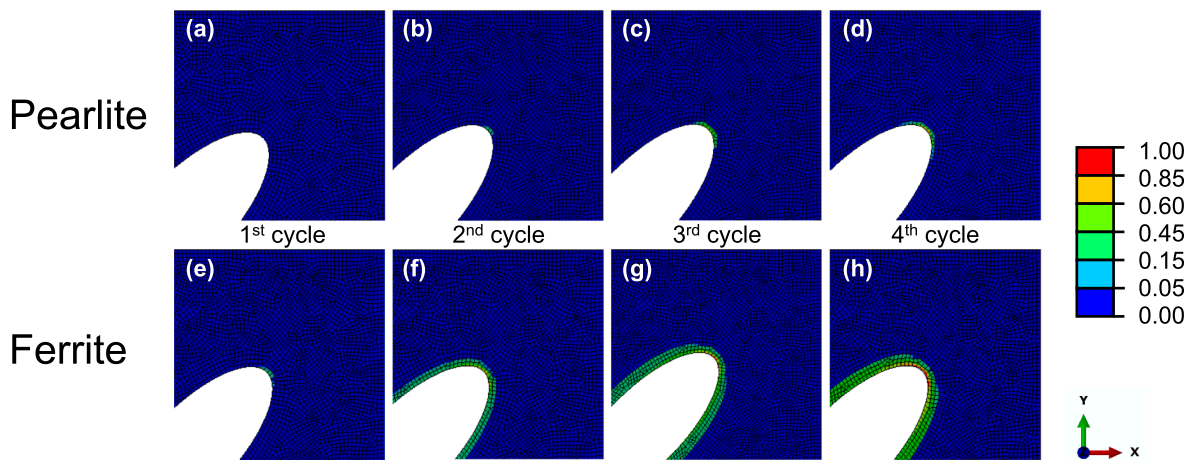

Fig. 6. Evolution of plastic zone in RVE with thermal cycles for vermicular inclusion: (a)-(d) pearlitic layer; (e)-(h) ferritic layer.
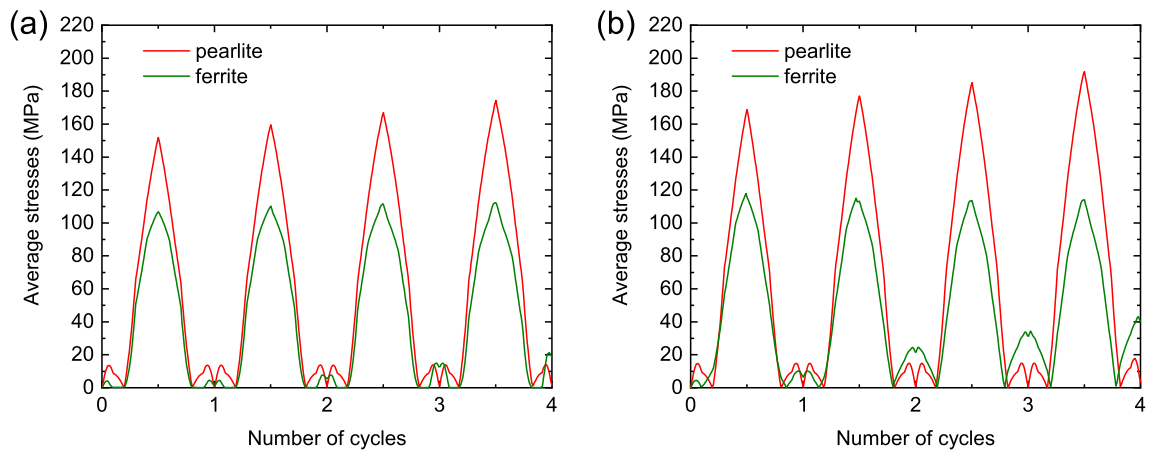

Fig. 7. Average value of residual stresses developed during four thermal cycles in ferritic and pearlitic domains for nodular (a) and vermicular (b) inclusion.

in the following thermal cycles, and for the case of the ferritic layer, the residual stresses developed at the end of the first cycle were around 25 MPa, much higher compared to those in the pearlitic layer at the same stage, that were less than 7.5 MPa (Fig. 7a). Considering this along with the fact that the yield point of ferrite is much lower than that of pearlite, the earlier onset of plasticisation in the ferritic layer was justified. The magnitude of the developed plastic strains was around 23% of the maximum plastic strain at 500 °C, and these appeared at the inner circumference of the ferritic area. At the end of the third thermal cycle, the plastic zone evolved and almost doubled in size. The magnitude of plastic strains ranged now from 75% up to 87% of the maximum plastic strain at 500 °C (Fig. 5g). At the end of the fourth cycle, the size of plastic zone was almost 1.5 times larger compared to the corresponding at the end of the previous cycle. The maximum plastic strains were developed near the circumference, where graphite was in contact with the ferritic layer. The evolution of the plastic zone after each cycle was mainly attributed to the residual stresses developed after each cycle. As for the case of ferrite, the magnitude of residual stresses in the ferritic layer was amplified after each cycle, causing expansion of the plastic zone (Fig. 7a).

Although the protective effect of the surrounding layer was also confirmed for the vermicular inclusion, the profile of developed plastic strains was significantly different. More specifically, for a pearlitic layer around a vermicular inclusion, plasticisation did not happen during the first thermal cycle, appearing during the second thermal cycle at the edges of the vermicular inclusion. Despite the high yield point of pearlite, sharp edges of a vermicular inclusion act as stress concentrators; hence, the stresses developed in this area exceeded the yield point causing the onset of plasticisation. Their magnitude was around 10% of the maximum plastic strain developed in the ferritic layer of a nodular inclusion at 500 °C. At the end of the third thermal cycle, the area of the plastic zone became five times larger, and the magnitude of strains reached 42% of the maximum plastic strain in the ferritic layer of a nodular inclusion at 500 °C. Finally, at the end of the fourth cycle, the size of the plastic zone grew some two times compared to that of the previous cycle and developed strains were almost 70% of the maximum plastic strain in the ferritic layer of a nodular inclusion at 500 °C. The growth of the plastic zone after each thermal cycle can be still attributed to the residual stresses, which for the case of the vermicular inclusion surrounded by the pearlitic layer were much higher compared to the corresponding ones for the nodular particle surrounded by the same layer. This can be explained by the effect of the complex shape of the vermicular inclusion in the distribution of stresses in the RVE.

Moreover, the case of ferritic layer around the vermicular inclusion demonstrated the plasticisation even from the first thermal cycle (Fig. 6e). This can be attributed not only to the lower yield point of ferrite but also to the stress concentration around the vertex area of the vermicular inclusion, with the magnitude exceeding the yield point of ferrite, causing the initiation of plasticisation. The
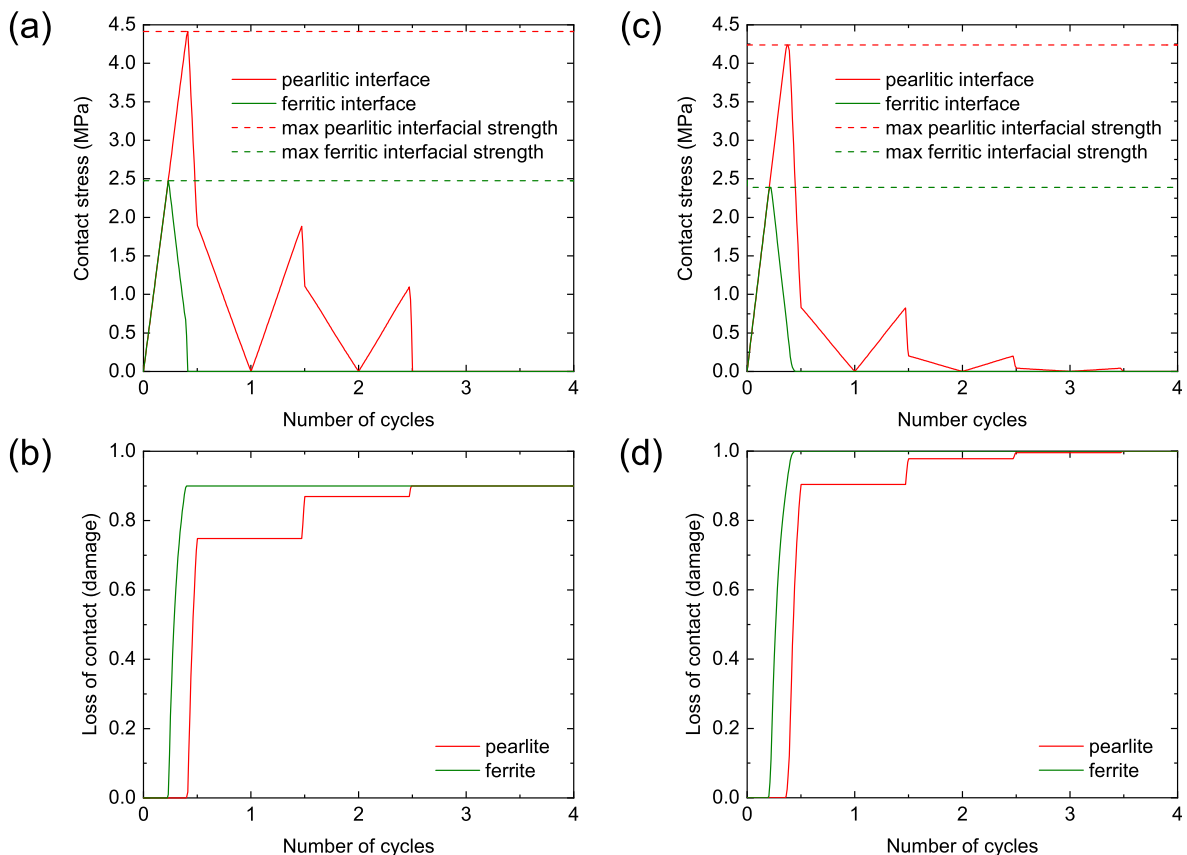

Fig. 8. Onset and further evolution of thermal debonding in a pearlitic and ferritic matrix for nodular (a), (b) and vermicular (c), (d) inclusion.

magnitude of the developed plastic strains was less than 10% of the maximum plastic strain in the ferritic layer of a nodular inclusion at 500 °C. At the end of the second thermal cycle, the plastic zone covered almost 50% of the inner elliptical circumference of the ferritic layer, and the plastic strains reached some 45% of the maximum plastic strain in the ferritic layer of a nodular inclusion at 500 °C (Fig. 6f). At the end of the third and fourth thermal cycles, the plastic zone covered around 75% and 95% of the ferritic layer, respectively. Higher plastic strains were observed at the edges of the inclusion; their magnitude increased from 80% during the third thermal cycle up to 100% at the end of the fourth (Fig. 6g and h). The growth of the plastic zone after each thermal cycle can also be attributed to both the residual stresses and the stress concentration due to the distinctive geometry of the inclusion.

It is evident that plastic deformations appeared earlier in the ferritic layer compared to the pearlitic one, regardless of the morphology of the inclusion examined. Ferrite is softer, with a lower yield point and a higher CTE compared to pearlite. As the temperature increased, the ferritic layer deformed more compared to the inclusion due to the mismatch of the CTEs, inducing stresses that exceeded the yield point of ferrite causing plasticisation. On the other hand, pearlite has a higher yield point and a lower CTE; therefore, the stresses developed due to the mismatch were lower and did not exceed the pearlitic yield point. Plasticisation was accelerated when the shape of the inclusion diverges from the spherical, regardless of the nature of the surrounding layer. As the shape of the inclusion became more elliptical, its vertices became sharper, acting as stress concentrators, causing the development of high stresses in those areas, thus accelerating the onset of plasticisation. Considering these two parameters, it can be concluded that the most prone to plasticisation configuration is a vermicular inclusion surrounded by a ferritic matrix and the least a nodular particle with pearlite around it.

3.2. Thermal debonding

The effect of the surrounding layer on decohesion of graphite is investigated in this section. The CTEs of graphite, pearlite, and ferrite differ; more specifically, that of graphite is an order of magnitude smaller than that of the other two, which are only slightly different. This mismatch causes graphite decohesion as the temperature of the unit cell increases since graphite cannot expand as much and as quickly as its surrounding layer. The results of this investigation are depicted in Fig. 8.

The surrounding layer of a spherical inclusion influences the onset and further propagation of graphite decohesion. More specifically, decohesion initiated earlier when the surrounding layer was ferritic. As discussed in the previous section, the CTE for ferrite is higher than that of pearlite; hence, the ferritic layer expanded more than the pearlitic one, triggering graphite debonding in the first thermal cycle (Fig. 8a and b). In Fig. 8a, the contact stress in debonded areas is depicted. As the temperature increased, the contact stress increased as well to maintain bonding until it reached a critical value corresponding to the ultimate strength of the interface. After this point, the interface could not bear any further tensile load and the gradual degradation of bonding started. As the bonding between the two constituents became more and more weak, the magnitude of contact stress decreased. A zero-contact stress means that graphite was no longer in contact with the ferritic layer in the area, where the contact stress was measured. So, there was no interaction between these two constituents in this area, and no stresses or strains could be transferred. For the ferritic layer, full decohesion was observed in the areas close to the sharp edges of the ellipse, before the second thermal cycle (Fig. 8b).

The pearlitic layer around the nodular inclusion seems to protect some parts of the particle from being fully debonded in the first thermal cycle. The small difference in the CTEs for ferrite and pearlite led to a later initiation of debonding (Fig. 8). The mismatch between pearlite and graphite was not so pronounced as pearlite deforms less. Contact stress reached its maximum value during the first cycle, determining the onset of thermal debonding. A further rise in temperature caused the evolution of the phenomenon; however, full decohesion did not occur during this thermal cycle, since the loss of contact at the end of the loading stage of the first thermal cycle was around 72% (Fig. 8b). During unloading, an anticipated decrease of contact stress occurred as the RVE cooled down at this stage and no loading was applied directly to it. Following the mechanism described above, contact stresses started increasing again in the second thermal cycle, reaching its maximum value, which was now much lower compared to that of the first cycle (Fig. 8a). The strength of the interface decreased because of the interfacial damage accumulated in the first cycle. The loss of contact at the end of the second thermal cycle corresponded to around 80% (Fig. 8b); graphite decohesion finally took place during the third cycle (Fig. 8a and b).

Three observations should be discussed here. First, interfacial strength is linked to the surrounding layer and its mechanical properties. Therefore, a stronger interface was expected for the pearlitic layer and a weaker one for the ferritic. Secondly, debonding did not reverse during thermal unloading since it was not modelled to do so. There is some evidence that debonding can be reversed during unloading [37,38], however, this healing process was not considered in this study since the cohesive elements used did not perform under compression. Finally, the evolution of decohesion was not linear during subsequent cycles, as thermal debonding is a nonlinear phenomenon and the onset of plasticisation led to a nonlinear response.

The influence of different surrounding layers on debonding of the vermicular inclusion did not differ much from that of the spherical one. Debonding of the vermicular inclusion surrounded by the ferritic layer was observed before that for the pearlitic one. In the case of the vermicular inclusion, this can be attributed to the difference between the CTEs of the two matrix phases and to the particle shape. Following the same pattern described above, the initiation of debonding was defined when the contact stresses equalled the ultimate interfacial strength (Fig. 8c). For the case of the ferritic layer around the vermicular inclusion, this happened during the first thermal cycle (Fig. 8d). However, for the pearlitic layer, decohesion occurred gradually during the first three thermal cycles (Fig. 8c and d). Its initiation took place during the first thermal cycle, at a higher temperature than that for the ferritic layer since the pearlitic interface was stronger. The loss of contact was reported to be nearly 90% (Fig. 8d). During the second thermal cycle, the debonding evolved, causing an extra 10% of loss of contact. Finally, a full decohesion was observed at the end of the loading stage during the third cycle.

Directly comparing the responses of the nodular and of the vermicular particle surrounded by either pearlitic or ferritic layer arises a few interesting observations. The onset of debonding and matrix plasticisation started later for a nodular inclusion regardless of the layer surrounding it. This is attributed to the irregular shape of a vermicular particle. The sharper edges of a vermicular particle triggered a stress concentration around them (Fig. 9). This concentration led to the earlier initiation of both plasticisation and decohesion (Table 5).

4. Discussion

4.1. Modelling without surrounding layer

A comparison of behaviours of RVEs without direct introduction of a specific layer around the particles and the ones studied above is presented here. For this investigation, the RVE enclosed a single vermicular inclusion. Obviously, modelling the surrounding matrix as a homogenised medium, instead of considering the phases, is easier to handle computationally and does not require microscale experiments to determine the constitutive parameters for each phase.

In the former RVEs no plasticisation was observed since the von Mises stresses in the entire matrix area were significantly below the yield point of matrix material (Fig. 10). Not only the RVE was formed by two domains with different thermomechanical properties (rather than three in Section 3) but also the macroscopic CTE of CGI is lower than that of both phases thanks to the contribution of other graphite particles, accounted implicitly in the homogenised medium. As a result, the mismatch of the CTEs of graphite and the matrix was lower resulting in the development of stresses with a magnitude not high enough to cause plasticisation in any cycle.

Graphite debonding for the RVE without phases initiated during the first cycle, however, both the respective temperature and further evolution of debonding were different from those in simulations with matrix phases. Here, the decohesion started at 255 °C, i. e., much higher than the corresponding temperature for ferrite and much lower than that for pearlite.

4.2. Effect of temperature-dependent constitutive parameters

A comparison for RVEs with temperature-independent data for the matrix phases is presented in this section. For this investigation, the RVE had a single vermicular inclusion surrounded by a ferritic or a pearlitic layer, and the Young's modulus, the CTE, and the plastic curve for each matrix phase were those obtained at room temperature. Modelling the matrix phases with temperature-independent constitutive parameters reduced computational time and did not require conducting experiments at high temperatures.

The obtained results (Table 6) for temperature-independent formulation demonstrated that the onset of decohesion took place at exactly the same temperature as when temperature-independent data were used. However, the evolution of decohesion was affected by the selection of constitutive parameters, namely, when the temperature-independent data were used, the CTE of metallic domains did not increase with temperature. Hence, the mismatch with the corresponding one of graphite did not exacerbate, causing no further propagation of decohesion.

Further, matrix plasticisation was primarily influenced by the selection of constitutive parameters used for the pearlitic and ferritic layers. When temperature-independent constitutive data were used, neither the Young's modulus nor the yield point decreased as the temperature increased. Therefore, the developed stresses were not high enough to exceed the yield point and cause the appearance of plastic strains in the matrix areas of the RVE. However, when temperature-dependent data were used, matrix plasticisation was observed, because as the yield point decreased, the material of the surrounding layer became softer allowing the developed stress to cause plasticisation.

5. Conclusions

The influence of matrix phases – ferrite or pearlite – on thermal debonding of graphitic inclusions in CGI was investigated in this study. After performing thermal cycles on a CGI specimen to confirm thermal debonding experimentally, a micromechanical approach was adopted for the development of a numerical model, where a two-dimensional RVE comprising single inclusions surrounded by an interfacial layer to account for decohesion was generated. To investigate the effect of matrix phases, an outer layer was added and assigned with the properties of either ferrite or pearlite. An elastoplastic constitutive law was assumed for all constituents, whereas the interfacial layer was modelled with cohesive elements, associated with a damage criterion to consider debonding. The influence of matrix phases was studied for two graphite morphologies, a nodular and a vermicular particle. The effect of employing temperature-dependent or independent data for pearlite and ferrite on the response of the unit cell was also investigated.

A few interesting points were derived from this study:

- A shielding effect was evident when a pearlitic layer surrounded the graphite inclusion, decelerating the onset of debonding since the mismatch of the CTEs for the two constituents was less pronounced.
- The process of matrix plasticisation also decelerated when a pearlitic layer was around graphite inclusions, mainly thanks to: (i) the lower mismatch of the CTEs of the two constituents that induced lower stresses in the RVE and (ii) the higher yield point of pearlite.
- Both graphite decohesion and matrix plasticisation initiated at temperatures between those for RVEs with a ferric or pearlitic outer layer, when models without separate layers around the inclusion were used.
- Finally, the use of temperature-independent constitutive data for the matrix phases affected only the onset of matrix plasticisation. Simplification of the models – disregarding the specific microstructure or temperature dependence of microconstituent's
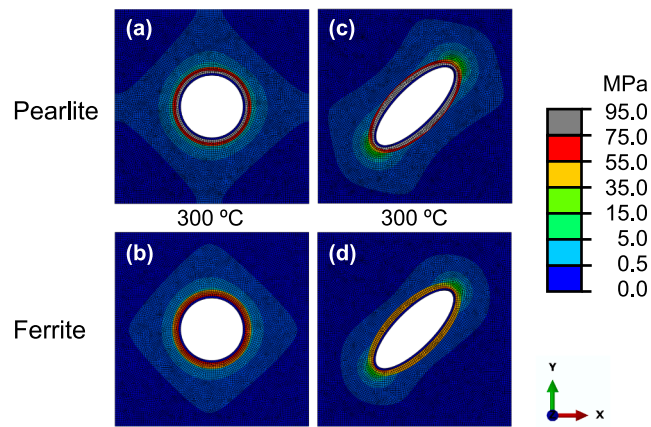
Fig. 9. Stress distribution for the 1st cycle for nodular (a, b) and vermicular (c, d) inclusion surrounded by different matrix phases.

Table 5
Onset of plasticisation and damage for nodular and vermicular inclusions and different surrounding layers.

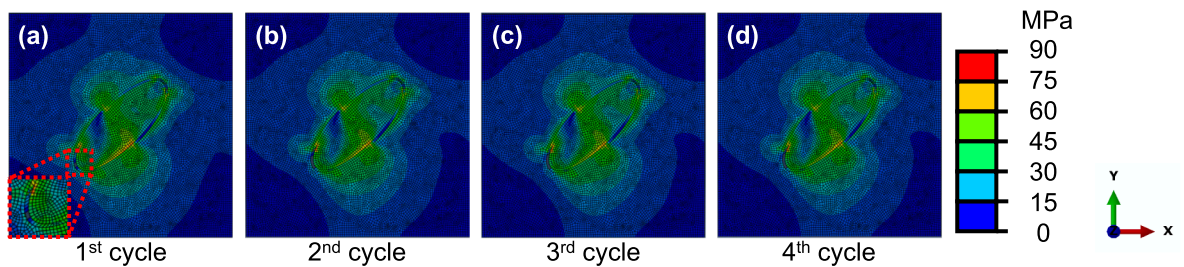|	Damage initiation	Full debonding	Matrix plasticisation
Pearlite			
Nodular	1st cycle, 416 °C	3rd cycle, 492 °C	4th cycle, 410 °C
Vermicular	1st cycle, 397 °C	4th cycle, 492 °C	2nd cycle, 492 °C
Ferrite			
Nodular	1st cycle, 254 °C	1st cycle, 406 °C	2nd cycle, 400 °C
Vermicular	1st cycle, 180 °C	1st cycle, 473 °C	1st cycle, 492 °C

Fig. 10. Distribution of von Mises stress at 500 °C of various cycles in RVE with single vermicular inclusion (no separate matrix phases considered). Deleted elements at the interface correspond to full debonding.

Table 6
Onset of decohesion and matrix plasticisation for RVEs with temperature-dependent and -independent data for pearlite and ferrite.

	Onset of decohesion	Full debonding	Matrix plasticisation
Pearlite			
Temperature-independent	1st cycle, 482 °C	–	–
Temperature-dependent	1st cycle, 482 °C	4th cycle, 492 °C	2nd cycle, 492 °C
Ferrite			
Temperature-independent	1st cycle, 235 °C	–	–
Temperature-dependent	1st cycle, 235 °C	1st cycle, 406 °C	1st cycle, 492 °C

mechanical data – provides an inadequate assessment of the processes affecting structural integrity such as plasticisation or microcracking.

Declaration of Competing Interest

The authors declare that they have no known competing financial interests or personal relationships that could have appeared to influence the work reported in this paper.

References

[1] S. Dawson, Compacted graphite iron – A material solution for modern diesel engine cylinder blocks and heads, China foundry, 241–6, 2009.

[2] W.J. Yang, J.C. Pang, L. Wang, S.G. Wang, Y.Z. Liu, L. Hui, S.X. Li, Z.F. Zhang, Tensile properties and damage mechanisms of compacted graphite iron based on microstructural simulation, Mater. Sci. Eng. A 814 (2021) 141244, https://doi.org/10.1016/j.msea.2021.141244.

[3] G. Nicoletto, L. Collini, R. Konečná, P. Bujnová, Strain heterogeneity and damage localization in nodular cast iron microstructures, Mater. Sci. Forum 482 (2009) 255–258.

[4] Y. Qiu, J.C. Pang, E.N. Yang, S.X. Li, Z.F. Zhang, Transition of tensile strength and damaging mechanisms of compacted graphite iron with temperature, Mater. Sci. Eng. A 677 (2016) 290–301.

[5] Y. Qiu, J.C. Pang, S.X. Li, E.N. Yang, W.Q. Fu, M.X. Liang, Z.F. Zhang, Influence of thermal exposure on microstructure evolution and tensile fracture behaviors of compacted graphite iron, Mater. Sci. Eng. A 664 (2016) 75–85.

[6] R.W. Gregorutti, J.E. Grau, Mechanical properties of compacted graphite cast iron with different microstructures, Int. J. Cast Met. Res. 27 (5) (2014) 275–281.

[7] B. Šamec, I. Potrč, M. Šraml, Low cycle fatigue of nodular cast iron used for railway brake discs, Eng. Fail. Anal. 18 (6) (2011) 1424–1434.

[8] M. Pevec, G. Oder, I. Potrč, M. Šraml, Elevated temperature low cycle fatigue of grey cast iron used for automotive brake discs, Eng. Fail. Anal. 42 (2014) 221–230.

[9] V. Di Cocco, F. Iacoviello, M. Cavallini, Damaging micromechanisms characterization of a ferritic ductile cast iron, Eng. Fract. Mech. 77 (11) (2010) 2016–2023.

[10] F. Iacoviello, V. Di Cocco, A. Rossi, M. Cavallini, Damaging micromechanisms characterization in pearlitic ductile cast irons, Procedia Mater. Sci. 3 (2014) 295–300.

[11] Y. Qiu, J.C. Pang, S.X. Li, M.X. Zhang, Z.F. Zhang, Influence of temperature on the low-cycle fatigue properties of compacted graphite iron, Int. J. Fatigue 112 (2018) 84–93.

[12] C.L. Zou, J.C. Pang, M.X. Zhang, Y. Qiu, S.X. Li, L.J. Chen, J.P. Li, Z. Yang, Z.F. Zhang, The high cycle fatigue, deformation and fracture of compacted graphite iron: Influence of temperature, Mater. Sci. Eng. A 724 (2018) 606–615.

[13] Y. Qiu, J.C. Pang, C.L. Zou, M.X. Zhang, S.X. Li, Z.F. Zhang, Fatigue strength model based on microstructures and damage mechanism of compacted graphite iron, Mater. Sci. Eng. A 724 (2018) 324–329.

[14] P.V. McLaughlin, R.E. Frishmuth, Failure analysis of cast irons under general three dimensions stress state, J. Eng. & Tech., 69–75, 1976.

[15] B.L. Josefson, U. Stigh, H.E. Hjelm, A nonlinear kinematic hardening model for elastoplastic deformations in grey cast iron, J. Eng. Mater. Technol. Trans. ASME 117 (2) (1995) 145–150.

[16] B.L. Josefson, H.E. Hjelm, Modelling elastoplastic deformations in grey cast iron, in: K.T. Rie (Ed.), Low Cycle Fatigue and Elasto-Plastic Behaviour of Materials, Springer, Dordrecht, 1992, pp. 465–472.

[17] H.E. Hjelm, Yield surface for grey cast iron under biaxial stress, J. Eng. Mater. Technol. 3 (1994) 465–472.

[18] B.L. Josefson, U. Stigh, H.E. Hjelm, A nonlinear kinematic hardening model for elastoplastic deformations in grey cast iron, J. Eng. Mater. Technol. 117 (1995) 145–150.

[19] H. Altenbach, G.B. Stoychev, K.N. Tushtev, On elastoplastic deformation of grey cast iron, Int. J. Plast. 17 (5) (2001) 719–736.

[20] Y.Y. Zhang, J.C. Pang, R.L. Shen, Y. Qiu, S.X. Li, Z.F. Zhang, Investigation on tensile deformation behavior of compacted graphite iron based on cohesive damage model, Mater. Sci. Eng. A 713 (2018) 260–268.

[21] M. Metzger, T. Seifert, Computational assessment of the microstructure-dependent plasticity of lamellar gray cast iron - Part I: Methods and microstructure-based models, Int. J. Solids Struct. 66 (2015) 184–193.

[22] M. Metzger, T. Seifert, Computational assessment of the microstructure-dependent plasticity of lamellar gray cast iron - Part III: A new yield function derived from microstructure-based models, Int. J. Solids Struct. 66 (2016) 194–206.

[23] T. Andriollo, J. Thorborg, N.S. Tiedje, J. Hattel, Modeling of damage in ductile cast iron - the effect of including plasticity in the graphite nodules, IOP Conf. Ser. Mater. Sci. Eng. 84 (2015) 12–27.

[24] T. Andriollo, J. Thorborg, J. Hattel, Modeling the elastic behavior of ductile cast iron including anisotropy in the graphite nodules, Int. J. Solids Struct. 100-101 (2016) 523–535.

[25] British Standards Institution, BS EN 16079. Founding. Compacted (vermicular) graphite cast irons, 2011.

[26] D.M. Stefanescu, Solidification of metal matrix composites, in: D.M. Stefanescu (Ed.), Science and Engineering of Casting Solidification, Springer International Publishing, Cham, 2015, pp. 305–341, https://doi.org/10.1007/978-3-319-15693-4_15.

[27] R. Hill, Elastic properties of reinforced solids: Some theoretical principles, J. Mech. Phys. Solids 11 (5) (1963) 357–372.

[28] F.A. Cerqueira, A.S. Nishikawa, W.L. Guesser, C.R.d.F. Azevedo, Three-dimensional reconstruction of compacted graphite in vermicular cast iron by manual serial sectioning, Rev. Esc. Minas 68 (3) (2015) 307–312.

[29] C. Xu, T. Wigger, M.A. Azeem, T. Andriollo, S. Fæster, S.J. Clark, Z. Gong, R. Atwood, J.-C. Grivel, J.H. Hattel, P.D. Lee, N.S. Tiedje, Unraveling compacted graphite evolution during solidification of cast iron using in-situ synchrotron X-ray tomography, Carbon 184 (2021) 799–810.

[30] E.N. Palkanoglou, K.P. Baxevanakis, V.V. Silberschmidt, Interfacial debonding in compacted graphite iron: effect of thermal loading, Procedia Struct. Integr. 28 (2020) 1286–1294.

[31] P. Tao, J.-M. Gong, Y.-F. Wang, Y. Jiang, Y. Li, W.-W. Cen, Characterization on stress-strain behavior of ferrite and austenite in a 2205 duplex stainless steel based on nanoindentation and finite element method, Results Phys. 11 (2018) 377–384.

[32] V.V. Silberschmidt, E. Werner, Analysis of thermal residual stresses in duplex-type materials, Comput. Mater. Sci. 16 (1-4) (1999) 39–52.

[33] E.J. Seldin, Stress-strain properties of polycrystalline graphites in tension and compression at room temperature, Carbon 4 (2) (1966) 177–191.

[34] W.L. Greenstreet, G.T. Yahr, R.S. Valachovic, The behavior of graphite under biaxial tension', Carbon 11 (1) (1973) 43–57.

[35] A. Drago, M. Pindera, Micro-macromechanical analysis of heterogeneous materials: Macroscopically homogeneous vs periodic microstructures, Compos. Sci. Technol. 67 (6) (2007) 1243–1263.

[36] F. Iacoviello, O. Di Bartolomeo, V. Di Cocco, V. Piacente, Damaging mechanisms in ferritic-pearlitic ductile cast irons, Mater. Sci. Eng. A 478 (1-2) (2008) 181–186.

[37] F. Iacoviello, V. Di Cocco, M. Cavallini, Fatigue crack propagation and overload damaging micromechanisms in a ferritic–pearlitic ductile cast iron, Fatigue Fract. Eng. Mater. Struct. 39 (2016) 999–1011.

[38] C.L. Zou, J.C. Pang, Y. Qiu, R. Liu, S.X. Li, G.X. Jing, C.G. Xu, Z.F. Zhang, The high-cycle fatigue fracture mechanism and fatigue strength prediction of compacted graphite iron, International Journal of Fatigue 161 (2022) 106881, https://doi.org/10.1016/j.ijfatigue.2022.106881.